JPE 19-2-5

https://doi.org/10.6113/JPE.2019.19.2.380
ISSN(Print): 1598-2092 / ISSN(Online): 2093-4718

Analysis and Design of Function Decoupling High Voltage Gain DC/DC Converter

Yuqi Wei*, Quanming Luo†, Xingyu Lv*, Pengju Sun*, and Xiong Du*

†,*Department of Electrical Engineering, Chongqing University, Chongqing, China

Abstract

Traditional boost converters have difficulty realizing high efficiency and high voltage gain conversion due to 1) extremely large duty cycles, 2) high voltage and current stresses on devices, and 3) low conversion efficiency. Therefore, a function decoupling high voltage gain DC/DC converter composed of a DC transformer (DCX) and an auxiliary converter is proposed. The role of DCX is to realize fixed gain conversion with high efficiency, whereas the role of the auxiliary converter is to regulate the output voltage. In this study, different forms of combined high voltage gain converters are compared and analyzed, and a structure is selected for the function decoupling high voltage gain converter. Then, topologies and control strategies for the DCX and auxiliary converter are discussed. On the basis of the discussion, an optimal design method for circuit parameters is proposed, and design procedures for the DCX are described in detail. Finally, a 400 W experimental prototype based on the proposed optimal design method is built to verify the accuracy of the theoretical analysis. The measured maximum conversion efficiency at rated power is 95.56%.

Key words: Function decoupling, High voltage gain, High efficiency, LLC resonant converter

I. INTRODUCTION

Environmental problems and shortage of fossil energy have resulted in increased demand for renewable energy, such as solar and wind energy [1], [2]. Distributed photovoltaic (PV) systems have been widely used due to their superior reliability and efficiency. However, the input voltage (380-400 V) of a grid-connected inverter is much higher than the output voltage of a PV array (40-60 V). Therefore, a step-up DC/DC converter is required to realize voltage matching.

The most fundamental step-up converter is the boost converter. Theoretically, a boost converter can have infinite voltage gain when its duty cycle is close to unity; however, when parasitic parameters are considered, boost converter operation is suitable only under conditions with voltage gains less than four, and it cannot satisfy the requirements of PV system. To achieve high efficiency and high gain conversion, substantial research on this topic has been published. Nonisolated high step-up converters can be divided into three types: I) switched-capacitor or switched-inductor high step-up converters [3], [4], in which high voltage ratio is realized by combining a single or several switched-capacitor or switched-inductor units with a basic DC/DC converter; II) coupled-inductor high step-up converters [5], in which voltage gain depends on the duty cycle and turns ratio of the coupled inductor; III) combined high step-up converters [6], in which voltage gain is improved by combing several basic DC/DC converters. For type I, the voltage gain is related to the number of switched-capacitor or switched-inductor units; therefore, in relatively high voltage gain applications, the complexity of the circuit is increased; in addition, the voltage gain can only be an integer, which limits its application. For type II, the voltage stress on devices and losses are increased due to resonance between the leakage inductance of the coupled inductor and the parasitic capacitance of switches or diodes; passive and active methods should be adopted to suppress the voltage spike caused by resonance. Type III maximizes the advantages of basic DC/DC converters; at the same time, the system structure can be simplified by sharing components. In addition, in some studies that focused on the combination of different techniques, such as [7] and [8], coupled inductor and switched capacitor techniques are adopted together to enhance performance, which is also a good solution. Overall, type III is a competent

Manuscript received Oct. 9, 2018; accepted Jan. 5, 2019
Recommended for publication by Associate Editor Hongfei Wu.
†Corresponding Author: lqm394@126.com
Tel: +86-13883730529, Chongqing University
*Department of Electrical Engineering, Chongqing University, China

solution, and the proposed converter belongs to this type.

Combined high voltage gain converters mainly have two different forms: cascaded and input-parallel output-series (IPOS) forms. Voltage gain is the square of a basic converter for the cascaded form; it can achieve high voltage gain with low duty cycle [9], [10]; however, back-end converters have high voltage stress. For the IPOS form, voltage gain is the sum of two basic converters; it can not only improve system voltage gain but also reduce voltage stress; boost-flyback [11], boost-SEPIC [12], boost-zeta [13], and flyback-SEPIC [14] all belong to this type.

In this study, an IPOS function decoupling high gain converter composed of a DC transformer (DCX) and an auxiliary converter is proposed. The rest of this paper is organized as follows. In Section II, analysis and comparison between cascaded and IPOS forms are presented according to system voltage gain and conversion efficiency, and the structure of the proposed function decoupling high gain converter is presented. The topology selection and control strategy for each unit are discussed in Section III. In Section IV, the proposed optimal design method is introduced, and the detailed design procedures are presented. Experimental results are analyzed in Section V. Finally, conclusions are drawn in Section VI.

II. Analysis of Two Forms of Combined High Voltage Gain Converter

In this section, analysis and comparison between two forms of combined high gain converters are presented. Figs. 1 and 2 show the structures of the cascaded and IPOS forms, respectively.

The voltage gains of the two converter units are M1 and M2, and their efficiencies are η1 and η2. From Fig. 1, the voltage gain and efficiency for the cascaded form can be obtained.

$$M_{\text{casc}} = M_1 M_2 \tag{1}$$

$$\eta_{\text{casc}} = \eta_1 \eta_2 \tag{2}$$

Similarly, from Fig. 2, the voltage gain and efficiency for the IPOS form can be derived as

$$M_{\text{ipos}} = M_1 + M_2, \tag{3}$$

$$\eta_{\text{ipos}} = \frac{P_{\text{o1}} + P_{\text{o2}}}{P_{\text{in1}} + P_{\text{in2}}} = \eta_1 \frac{P_{\text{in1}}}{P_{\text{in}}} + \eta_2 \frac{P_{\text{in2}}}{P_{\text{in}}}. \tag{4}$$

For the sake of analysis, the following assumptions are made: 1) $M_1 \in [0, 5]$, $M_2 \in [0, 5]$; 2) $\eta_1 \in [0.8, 1)$, $\eta_2 \in [0.8, 1)$. On the basis of the assumptions and Equations (1) and (3), Fig. 3, which shows the voltage gain comparison between the two forms, can be obtained. When M_1 and M_2 are lower than 1, M_{ipos} is higher than M_{casc}; when M_1 and M_2 are greater than 1, M_{casc} is higher than M_{ipos}.

A comparison of efficiency between the two forms based on

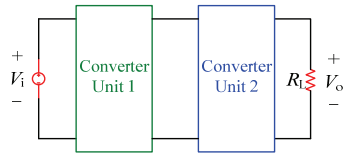

Fig. 1. Structure of the cascaded form.

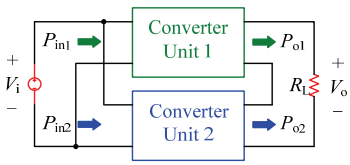

Fig. 2. Structure of the IPOS form.

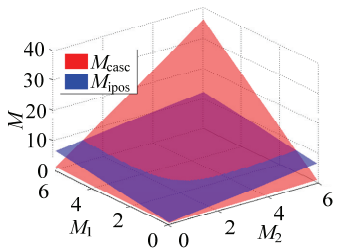

Fig. 3. Comparison of voltage gain between cascaded and IPOS forms.

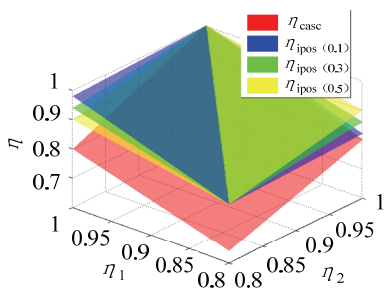

Fig. 4. Comparison of efficiency between cascaded and IPOS forms.

Equations (2) and (4) is shown in Fig. 4. The blue, green, and yellow curves illustrate when $P_{\text{in1}}/P_{\text{in}}$ equals 0.1, 0.3, and 0.5, respectively. Under these conditions, the efficiency of the IPOS form is higher than that of the cascaded form. In addition, for the IPOS form, the higher the power that is handled by the high-efficiency power conversion unit, the higher the overall system efficiency.

According to the above analysis, even though the IPOS form cannot achieve high voltage gain conversion, its voltage gain characteristic can satisfy PV system requirements, and it has better system efficiency than does the cascaded form. Therefore, the IPOS form is more advantageous than the cascaded form in PV system application.

DCX can achieve high efficiency and constant voltage gain conversion [15], [16]; thus, it is selected to handle as much power as possible. Voltage regulation is realized by another converter unit, which is called auxiliary converter. The structure of the proposed function decoupling high gain

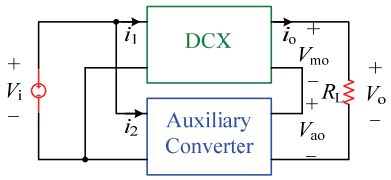

Fig. 5. Proposed function decoupling high gain converter structure.

converter is shown in Fig. 5.

Although the proposed converter has more components, it has the following advantages compared with a single LLC resonant converter.

1) It has high power handling ability, given the two units handling the total power.
2) Constant duty cycle and frequency operation can be implemented for the LLC resonant converter, whereas a variable switching frequency range is required for a single LLC resonant converter, which will complicate the magnetic components and electromagnetic interference (EMI) design.
3) Although the output voltage of an LLC converter can nearly remain constant at the resonant frequency operation point, this principle will be challenged during wide-range operation.

III. Topology Selection and Control Strategy

In this section, based on the functions of the DCX and auxiliary converter, the topology for each unit and corresponding control strategy are determined.

A. DCX

The role of DCX is to handle most of the power; high conversion efficiency is required to improve the overall system efficiency. Given that the outputs of DCX and auxiliary converter are in series connection, higher power handling ability means higher output voltage. Thus, a high gain conversion for DCX is also required. LLC resonant converters have been widely used in many applications due to their soft-switching capability in wide load ranges. However, frequency control strategy is often adopted to regulate output voltage, thereby complicating the optimal design of resonant components; in addition, system efficiency is reduced because of high reactive circulation current when the system operation point is far from the resonant operation point [17]. Fig. 6 shows an asymmetric half-bridge LLC resonant converter. DCX is not required to regulate output voltage; therefore, constant duty cycle and constant frequency operation can be implemented. On the one hand, by optimal design, zero-voltage switching (ZVS) operation for primary switches and zero-current switching (ZCS) operation for secondary diodes can be guaranteed; on the other hand, with the selection of a reasonable transformer turns ratio, high voltage gain conversion can be achieved, and

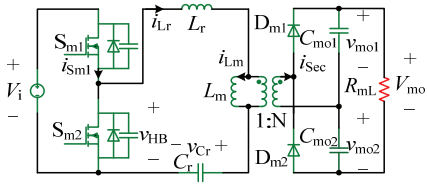

Fig. 6. Asymmetric half-bridge LLC resonant converter.

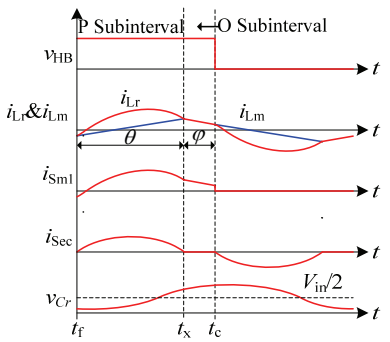

Fig. 7. Main waveforms during operation in PO mode.

voltage doublers composed of D_{m1}, D_{m2}, and C_{mo1}, C_{mo2} can further improve the system voltage gain. In addition, the leakage inductor of the transformer can be used as resonant inductor L_r, and L_m is the magnetic inductor of the transformer; thus, only resonant capacitor C_r is added into the circuit. This topology has high power density due to its high-frequency operation capability.

For LLC resonant converters, three subintervals exist during half of a switching period. During the positive of a half switching period, the P subinterval is defined when the voltage across the magnetic inductor is clamped by $V_{mo}/2N$; the N subinterval exists when the voltage across the magnetic inductor is clamped by $-V_{mo}/2N$; the O subinterval happens when no power flows to the secondary side of the transformer. Based on the sequences of these subintervals, an LLC resonant converter mainly has the following operation modes: PO, PON, PN, NP, NOP, and OPO. Take PO operation mode as an example. During half of the switching period, the LLC resonant converter operates at the P subinterval first, and then at the O subinterval.

Fig. 7 shows the main waveforms when an LLC resonant converter operates at PO mode. Before the drive signal of S_{m1} comes, the switch current i_{Sm1} is negative; thus, its parallel diode will be conducted, and ZVS operation for S_{m1} is achieved. Similarly, S_{m2} can achieve ZVS operation. According to the waveform of transformer secondary current i_{Sec}, the secondary diodes D_{m1} and D_{m2} can achieve ZCS operation. In other operation modes, such as PON, ZVS operation cannot be guaranteed for primary switches and leads to reduced efficiency; in OPO mode, three subintervals are involved, which complicates the mathematical derivation of this mode; in P mode, parasitic parameters and a slight variation of resonant components exist; thus, this operation cannot be

guaranteed. Therefore, the design consideration for DCX is to ensure that it can operate in PO mode during the entire operation.

When the operation point of an LLC resonant converter is close to the resonant frequency operation point, its voltage gain nearly remains constant with different input voltages and loads. Therefore, constant frequency and constant duty cycle operation are adopted for the converter to simplify the optimal design and the control circuit.

B. Auxiliary Converter

The output voltage of DCX varies with input voltage; thus, the role of the auxiliary converter is to regulate the output voltage. When the input voltage reaches the maximum value $V_{\text{in-max}}$, the output voltage of DCX also reaches the maximum value $V_{\text{mo-max}}$, whereas the output voltage of the auxiliary converter reaches its minimum value $V_{\text{ao-min}}$. For the sake of system efficiency, $V_{\text{ao-min}}$ is generally less than $V_{\text{in-max}}$; thus, the auxiliary converter needs to realize step-down conversion. When the input voltage reaches the minimum value $V_{\text{in-min}}$, the output voltage of DCX also reaches the minimum value $V_{\text{mo-min}}$, whereas the output voltage of the auxiliary converter reaches its maximum value $V_{\text{ao-max}}$. For wide input voltage applications, $V_{\text{ao-max}}$ is generally higher than $V_{\text{in-min}}$; thus, step-up conversion for the auxiliary converter is required.

Based on the above analysis, a noninverted buck-boost converter, as shown in Fig. 8, is selected for the auxiliary converter. In addition, it has the following advantages:

1) Compared with other step-up and step-down converters, such as buck-boost, cuk, and SEPIC, it has lower voltage stress;
2) Two switches S_{a1} and S_{a2} are present in the topology, and they can work simultaneously or separately according to the requirements, thus improving the control freedom of the system; compared with the buck-boost converter, it has a wider output voltage range and lower inductor current ripple [18];
3) Compared with cuk, SEPIC, and zeta, the selected converter requires fewer passive components; thus, high power density conversion can be achieved [19];
4) The input and output of buck-boost and cuk are inverted, which complicates the corresponding power supply and drive circuit.

According to Fig. 8, when S_{a2} is off, the output voltage can be regulated by adjusting the duty cycle of S_{a1}, and the converter is working in buck mode; when S_{a1} is on, the output voltage is regulated by controlling S_{a2}, and the converter is working in boost mode. However, when the output voltage is close to the input voltage in both operation modes, extreme duty cycle will appear; specifically, in buck mode, the duty cycle of S_{a1} should be close to 1, and in boost mode, the duty cycle of S_{a2} should be zero. Therefore, when the converter voltage gain $M_a \in [0.8,1]$, the duty cycle of S_{a2} is set as

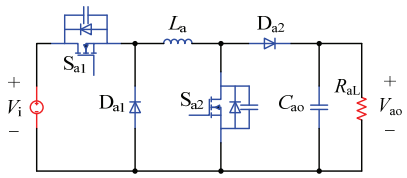

Fig. 8. Noninverted buck-boost converter.

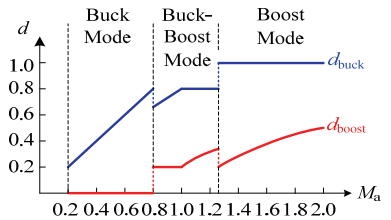

Fig. 9. Relationship between M_a, d_{Buck} and d_{Boost}.

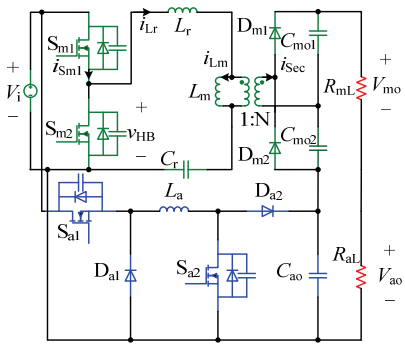

Fig. 10. Topology of the proposed converter.

d_{Boost}=0.2, whereas the duty cycle of S_{a1} $d_{\text{Buck}} \in [0.64,0.8]$; when the converter voltage gain $M_a \in [1,1.25]$, the duty cycle of S_{a1} is set as d_{Buck}=0.8, and the duty cycle of S_{a2} $d_{\text{Boost}} \in [0.2,0.36]$. Based on the above analysis, the relationship between the auxiliary converter voltage gain M_a and S_{a1}, S_{a2} duty cycle d_{Buck} and d_{Boost} can be obtained as shown in Fig. 9. With the adoption of this control strategy, the extreme duty cycle situation can be avoided, and the output voltage can be regulated.

The proposed converter topology is shown in Fig. 10.

IV. Optimal Design Method

In this section, the design considerations are presented. The design of DCX is the key point. Given the simplicity and the similarity of the design of the auxiliary converter to the traditional design, only the results are provided.

Fundamental harmonic analysis (FHA) is usually adopted to design an LLC resonant converter [20]. However, errors occur in this methodology [21], [22] due to the following assumptions.

1) The LLC resonant converter is always working in continuous conduction mode.
2) The input voltage of the resonant tank and the output voltage of the transformer are continuous square-

wave voltages that can be replaced by their fundamental harmonic components.

3) The equivalent AC resistance can be expressed as Rac=8n2RL/π2. With increased load, the error will further increase.

Therefore, in this study, an operation mode-based optimal design method is proposed. The precision of this method is highly improved compared with that of the FHA method.

The unknown parameters of DCX include transformer turns ratio N, resonant components L_r and C_r, and L_m. First, the transformer turns ratio N is determined according to the voltage gain of the DCX. Then, the resonant components are selected based on the proposed optimal design method. Finally, simulation cases are introduced to verify the theoretical analysis, and the design procedures are summarized.

The known parameters are V_i=40–60 V, V_o=400 V, P_o=100–400 W, f_s=100 kHZ.

A. Selection of Transformer Turns Ratio N

The voltage gain of the DCX is independent of the input voltage and load. When the input voltage reaches the maximum value $V_{in\text{-}max}$, the auxiliary converter operates in buck mode, and d_{buck} reaches the minimum value $d_{buck\text{-}min}$. To avoid extreme duty cycle, the following assumption is made:

$$d_{buck\text{-}min} \geq 0.2 . \tag{5}$$

According to Fig. 5, the following equation can be derived:

$$V_{in\text{-}max} d_{buck\text{-}min} + V_{in\text{-}max} M_m = V_o . \tag{6}$$

According to Equations (5) and (6), an inequality of M_m can be expressed as

$$M_m \leq 6.5 . \tag{7}$$

Similarly, when the input voltage equals the minimum value $V_{in\text{-}min}$, the auxiliary converter works in boost mode, and d_{boost} reaches the maximum value $d_{boost\text{-}max}$. To avoid extreme duty cycle, the following assumption is made:

$$d_{boost\text{-}max} \leq 0.8 . \tag{8}$$

According to Fig. 5, the following equation can be obtained:

$$\frac{V_{in\text{-}min}}{1\text{-}d_{boost\text{-}max}} + V_{in\text{-}min} M_m = V_o . \tag{9}$$

With the combination of Equations (8) and (9), another inequality of M_m can be obtained.

$$M_m \geq 5 \tag{10}$$

From Equations (7) and (10), M_m can be selected as

$$M_m = 6.5 . \tag{11}$$

The operating frequency is close to the resonant frequency; thus, the transformer turns ratio N is nearly the same as the voltage gain M_m.

$$N \approx M_m \tag{12}$$

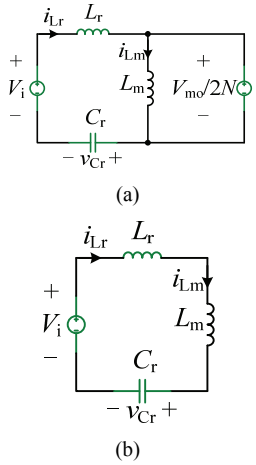

Fig. 11. Equivalent circuits of an LLC resonant converter. (a) In P subinterval. (b) In O subinterval.

In practice, the voltage gain is slightly higher than 1; finally, N=6.25 is selected.

B. Selection of Resonant Components

The design consideration for the resonant components is to ensure that the DCX is in PO mode during its entire operation, thus keeping its voltage gain constant.

First, parameters K, ω_r, and ω_m are defined as follows:

$$\begin{cases} K = \dfrac{L_m}{L_r} \\ \omega_r = \dfrac{1}{\sqrt{L_r C_r}} \\ \omega_m = \dfrac{1}{\sqrt{(L_r + L_m) C_r}} . \end{cases} \tag{13}$$

The equivalent circuits when the DCX operates in the P and O subintervals during the positive half of the switching period are shown in Figs. 11(a) and (b), respectively.

As shown in Fig. 11(a), when an LLC resonant converter operates in the P subinterval, the circuit can be described as

$$L_r C_r \frac{d^2}{dt^2} v_{Cr} + v_{Cr} = V_i - \frac{V_{mo}}{2N} . \tag{14}$$

The general solution for Equation (14) is

$$v_{Cr}(t) = k_1 \cos(\omega_r t) + k_2 \sin(\omega_r t) + V_i - \frac{V_{mo}}{2N} , \tag{15}$$

where k_1 and k_2 depend on the initial condition of the circuit.

According to Equation (15), the general solution for i_{Lr} can be derived as

$$i_{Lr}(t) = C_r \omega_r [-k_1 \sin(\omega_r t) + k_2 \cos(\omega_r t)] . \tag{16}$$

In the following section, the expressions of k_1 and k_2 are derived on the basis of the initial circuit condition.

According to Figs. 6 and 7, during half of the switching period, the voltage across the resonant capacitor increases

from $V_{Cr,tf}$ to $V_{Cr,tc}$. Therefore, the total charge of the resonant tank during this period can be expressed as

$$Q_{mi} = C_r\left(V_{Cr,tc} - V_{Cr,tf}\right). \quad (17)$$

Fig. 7 shows that $V_{Cr,tf}$ and $V_{Cr,tc}$ are symmetric with $V_i/2$; thus,

$$\frac{V_i}{2} - V_{Cr,tf} = V_{Cr,tc} - \frac{V_i}{2}. \quad (18)$$

With the combination of Equations (17) and (18), the total charge can be expressed as

$$Q_{mi} = C_r\left(V_i - 2V_{Cr,tf}\right). \quad (19)$$

The system efficiency is assumed to be 100%; thus, during one switching period, the input energy E_{mi} equals the output energy E_{mo}.

$$E_{mi} = E_{mo} \quad (20)$$

On the basis of the operation of the DCX, the following expressions for E_{mi} and E_{mo} can be obtained:

$$E_{mi} = V_i Q_{mi}, \quad (21)$$

$$E_{mo} = \frac{{V_{mo}}^2}{R_{mL} f_s}. \quad (22)$$

From Equations (19)–(22), the resonant capacitor voltage at t_f can be expressed as

$$V_{Cr,tf} = \frac{C_r R_{mL} V_i^2 f_s - V_{mo}^2}{2R_{mL} f_s C_r V_i}. \quad (23)$$

t_f is considered the initial point of the P subinterval; thus, $\omega_r t_f$=0 can be obtained. With substitution of this condition into Equation (15) and combination with Equation (23), the final expression for k_1 can be calculated as

$$k_1 = \frac{C_r R_{mL} V_{mo} V_i f_s - N C_r R_{mL} V_i^2 f_s - N V_{mo}^2}{2N R_{mL} f_s C_r V_i}. \quad (24)$$

According to Fig. 7, at t_f and t_x, the resonant inductor current i_{Lr} equals the magnetic inductor current i_m, that is,

$$\begin{cases} i_{Lr,tf} = i_{Lm,tf} \\ i_{Lr,tx} = i_{Lm,tx} \end{cases}. \quad (25)$$

The relationship between $i_{Lm,tx}$ and $i_{Lm,tf}$ can be described as

$$i_{Lm,tx} = i_{Lm,tf} + \frac{V_{mo}\theta}{2N\omega_r L_m}. \quad (26)$$

With the substitution of $\omega_r t_f$=0 and $\omega_r t_x = \theta$ into Equation (16) and their combination with Equations (25) and (26), respectively, the expression of k_2 can be solved as

$$k_2 = \frac{V_{mo}\theta}{2NK(\cos\theta - 1)} + \frac{\left(C_r R_{mL} V_{mo} V_i f_s - N C_r R_{mL} V_i^2 f_s - N V_{mo}^2\right)\sin\theta}{2N R_{mL} f_s C_r V_i(\cos\theta - 1)}. \quad (27)$$

The derivation for the P subinterval is thus completed. (The discussion of the O subinterval is similar to that of the P subinterval.)

From Fig. 11(b), the circuit can be described as

$$(L_r + L_m) C_r \frac{d^2}{dt^2} v_{Cr} + v_{Cr} = V_i. \quad (28)$$

The general solution for V_{cr} can be obtained as

$$v_{Cr}(t) = k_3 \cos(\omega_m t) + k_4 \sin(\omega_m t) + V_i. \quad (29)$$

From Equation (29), the general solution for i_{Lr} is derived as

$$i_{Lr}(t) = C_r \omega_m [-k_3 \sin(\omega_m t) + k_4 \cos(\omega_m t)]. \quad (30)$$

Similarly, k_3 and k_4 are determined on the basis of the initial circuit condition.

The resonant capacitor voltage V_{cr} at t_x calculated by two subintervals should be the same due to the continuity of V_{cr}. In the P subinterval, with the substitution of $\omega_r t_x = \theta$ into Equation (15), the resonant capacitor voltage at t_x can be expressed as

$$V_{Cr,tx} = k_1 \cos\theta + k_2 \sin\theta + V_i - \frac{V_{mo}}{2N}. \quad (31)$$

In the O subinterval, t_x is the initial point; with the substitution of $\omega_m t_x$=0 into Equation (29), the resonant capacitor voltage at t_x can be derived as

$$V_{Cr,tx} = k_3 + V_i. \quad (32)$$

From Equations (31) and (32), the following equation can be obtained:

$$k_3 = k_1 \cos(\theta) + k_2 \sin(\theta) - \frac{V_{mo}}{2N}. \quad (33)$$

Similarly, the resonant inductor current i_{Lr} at t_x calculated by two subintervals should be the same due to the continuity of i_{Lr}. In the P subinterval, with the substitution of $\omega_r t_x = \theta$ into Equation (16), the expression of the resonant inductor current at t_x can be derived as

$$I_{Lr,tx} = C_r \omega_r \left(-k_1 \sin\theta + k_2 \cos\theta\right). \quad (34)$$

In the O subinterval, with the substitution of $\omega_r t_x$ =0 into Equation (30), the expression of the resonant inductor current at t_x can be calculated as

$$I_{Lr,tx} = k_4 C_r \omega_m. \quad (35)$$

From Equations (13), (34), and (35), the following equation can be obtained:

$$k_4 = \sqrt{(K+1)}\left(-k_1 \sin\theta + k_2 \cos\theta\right). \quad (36)$$

From Equations (15), (16), (24), (27), (29), (30), (33), and (36), for quantitative calculation in PO mode, the relationship between C_r and θ needs to be determined.

With the substitution of $\omega_r t_f$=0 into Equation (15), the resonant capacitor voltage at t_f can be expressed as

$$V_{\mathrm{Cr,tf}} = k_1 + V_{\mathrm{i}} - \frac{V_{\mathrm{mo}}}{2N} . \tag{37}$$

With the substitution of $\omega_{\mathrm{m}}t_{\mathrm{c}}=\varphi$ into Equation (29), the resonant capacitor voltage at t_{c} can be calculated as

$$V_{\mathrm{Cr,tc}} = k_3 \cos\varphi + k_4 \sin\varphi + V_{\mathrm{i}} . \tag{38}$$

From Equations (18), (37), and (38), the following equation is obtained:

$$k_3 \cos\varphi + k_4 \sin\varphi = -k_1 + V_{\mathrm{i}} - \frac{V_{\mathrm{mo}}}{2N} . \tag{39}$$

Fig. 7 shows that the resonant inductor current value at t_{f} equals the value at t_{c} with the opposite sign; thus,

$$I_{\mathrm{Lr,tf}} + I_{\mathrm{Lr,tc}} = 0 . \tag{40}$$

In the P subinterval, with the substitution of t=0 into Equation (16), the resonant inductor current value at t_{f} can be calculated as

$$I_{\mathrm{Lr,tf}} = C_{\mathrm{r}}\omega_{\mathrm{r}}\left(-k_1 + k_2\right) . \tag{41}$$

In the O subinterval, with the substitution of $\omega_{\mathrm{m}}t_{\mathrm{c}}=\varphi$ into Equation (30), the resonant inductor current value at t_{c} can be calculated as

$$I_{\mathrm{Lr,tc}} = C_{\mathrm{r}}\omega_{\mathrm{m}}\left(-k_3 \sin\varphi + k_4 \cos\varphi\right) . \tag{42}$$

From Equations (13), (40), (41), and (42), the following equation is derived:

$$-k_3 \sin\varphi + k_4 \cos\varphi = \sqrt{K+1}\left(k_1 - k_2\right) . \tag{43}$$

With the combination of Equations (39) and (43), the following equation can be derived:

$$k_3{}^2 + k_4{}^2 = \left(K+1\right)\left(k_1 - k_2\right)^2 + \left(k_1 - V_{\mathrm{i}} + \frac{V_{\mathrm{mo}}}{2N}\right)^2 . \tag{44}$$

From Equations (24), (27), (33), (36), and (40), the relationship between C_{r} and θ can be derived as

$$\begin{aligned} & C_{\mathrm{r}}\begin{pmatrix} 4R_{\mathrm{mL}}M_{\mathrm{m}}f_{\mathrm{s}} / N - 4R_{\mathrm{mL}}M_{\mathrm{m}}{}^2 f_{\mathrm{s}} \\ + R_{\mathrm{mL}}f_{\mathrm{s}}\theta^2 + 4R_{\mathrm{mL}}f_{\mathrm{s}}\cos\theta \\ + R_{\mathrm{mL}}M_{\mathrm{m}}f_{\mathrm{s}}\theta^2 / N - \\ 4R_{\mathrm{mL}}M_{\mathrm{m}}\cos\theta / N + \\ R_{\mathrm{mL}}f_{\mathrm{s}}\theta^2\cos\theta + \\ R_{\mathrm{mL}}M_{\mathrm{m}}f_{\mathrm{s}}\theta^2\cos\theta / N - \\ 4R_{\mathrm{mL}}M_{\mathrm{m}}f_{\mathrm{s}}\theta\sin\theta / N \end{pmatrix} \\ & -\begin{pmatrix} 4M_{\mathrm{m}}{}^2 - 4NM_{\mathrm{m}} \\ + M_{\mathrm{m}}{}^2\theta^2 - 4M_{\mathrm{m}}{}^2\cos\theta \\ + 4NM_{\mathrm{m}}\cos\theta + \\ M_{\mathrm{m}}{}^2\theta^2\cos\theta - \\ 4M_{\mathrm{m}}{}^2\theta\sin\theta \end{pmatrix} = 0 \end{aligned} . \tag{45}$$

When the DCX is operating in PO mode, with a given resonant capacitor C_{r}, the corresponding θ can be calculated according to Equation (45). Then, given K, the values of k_1, k_2, k_3, and k_4 can be derived according to Equations (24), (27), (33), and (36), and the value of φ can be obtained on the basis of Equation (39) or (43). Finally, the quantitative calculation of the circuit can be performed.

From Fig. 7, the following expression can be obtained:

$$\frac{\theta}{\omega_{\mathrm{r}}} + \frac{\varphi}{\omega_{\mathrm{m}}} = \frac{1}{2f_{\mathrm{s}}} . \tag{46}$$

Equation (46) can be changed into the form of Equation (47).

$$\frac{\theta}{\omega_{\mathrm{r}}} + \frac{\varphi}{\omega_{\mathrm{r}}}\sqrt{K+1} = \frac{1}{2f_{\mathrm{s}}} \tag{47}$$

The values of θ and φ can be determined by the given C_{r} and K. Then, with the substitution of θ and φ into Equation (47), the value of ω_{r} can be obtained. Finally, according to Equation (13), the values of the resonant inductor L_{r} and magnetic inductor L_{m} can be calculated. The boundary condition and values of C_{r} and K need to be discussed to finalize the design.

According to [22], the adjunct operation modes of PO mode are the PON and OPO modes. The boundary condition between the PO and PON modes is as follows. When the DCX is operating in PO mode, at t_{c}, the voltage across the magnetic inductor $V_{\mathrm{Lm,tc}}$ equals $-V_{\mathrm{mo}}/2N$. Therefore, for operation in PO mode, the following inequality should be satisfied:

$$V_{\mathrm{Lm,tc}} \geq -\frac{V_{\mathrm{mo}}}{2N} . \tag{48}$$

When the DCX is operating in the O subinterval, according to the voltage divider law, the voltage across the magnetic inductor $V_{\mathrm{Lm,tc}}$ can be expressed as

$$V_{\mathrm{Lm,tc}} = \frac{K}{K+1}\left(V_{\mathrm{i}} - V_{\mathrm{Cr,tc}}\right) . \tag{49}$$

From Equations (18) and (49), the voltage across the magnetic inductor $V_{\mathrm{Lm,tc}}$ can be expressed as

$$V_{\mathrm{Lm,tc}} = \frac{K}{K+1}V_{\mathrm{Cr,tf}} . \tag{50}$$

With the combination of Equations (23), (48), and (50), the inequality of the load can be derived as

$$R_{\mathrm{mL}} \leq \frac{M_{\mathrm{m}}}{C_{\mathrm{r}}f_{\mathrm{s}}\left(\dfrac{1}{M_{\mathrm{m}}} + \dfrac{1}{NK} - \dfrac{1}{N}\right)} . \tag{51}$$

Similarly, the boundary condition between the PO and OPO modes can be described as follows. When the DCX is operating in PO mode, at t_{f}, the voltage across the magnetic inductor $V_{\mathrm{Lm,tf}}$ is $V_{\mathrm{mo}}/2N$. Therefore, for operation in PO mode, the following inequality should be satisfied:

$$L_{\mathrm{m}}\frac{di_{\mathrm{Lm}}}{dt}\Big|_{t=t_{\mathrm{f}}} = L_{\mathrm{m}}\frac{di_{\mathrm{Lr}}}{dt}\Big|_{t=t_{\mathrm{f}}} \geq \frac{V_{\mathrm{mo}}}{2N} . \tag{52}$$

With the combination of Equations (13), (16), (24), and (52),

the inequality of the load can be derived as

$$R_{\mathrm{mL}} \geq \frac{M_{\mathrm{m}}}{C_{\mathrm{r}} f_{\mathrm{s}} \left(\frac{1}{M_{\mathrm{m}}} + \frac{1}{NK} + \frac{1}{N} \right)}. \tag{53}$$

C. Parameter Design and Simulation Verification

On the basis of the above analysis, the proposed optimal design method can be summarized as follows.

1) According to the known parameters, the value of M_{m}, N and R_{mL} are determined.
2) According to Inequalities (51) and (53), the figures, which show the boundary condition of PO mode, are obtained. On the basis of the figures, the reasonable range of C_{r} and K can be found.
3) The range of C_{r} and K is further constrained by optimizing efficiency; one is the soft-switching capability, which is related to switching losses; the other is the RMS current of the resonant tank, which is related to the conduction losses.
4) Reasonable values of C_{r} and K based on 2) and 3) are selected.
5) Then, the value of θ can be calculated according to Equation (45).
6) The values for k_1, k_2, k_3, and k_4 are obtained on the basis of Equations (24), (27), (33), and (36).
7) The value of φ can be determined according to Equation (39) or (43).
8) The value of ω_{r} is calculated according to Equation (47).
9) The values of the resonant inductor L_{r} and magnetic inductor L_{m} can be determined according to Equation (13).

On the basis of the above analysis, M_{m}=6.5 and N=6.25 are selected. When the input voltage equals the maximum value $V_{\text{in-max}}$, the output voltage of the DCX reaches the maximum value $V_{\text{mo-max}}$. If the output current equals the minimum value $I_{\text{o-min}}$, then the equivalent resistance of the DCX reaches its maximum value $R_{\text{mL-max}}$, and it can be expressed as

$$R_{\text{mL-max}} = \frac{V_{\text{mo-max}}}{I_{\text{o-min}}} = \frac{M_{\mathrm{m}} V_{\text{i-max}} V_{\mathrm{o}}}{P_{\text{o-min}}} = 1560\Omega. \tag{54}$$

Similarly, the minimum value of R_{mL} can be derived as

$$R_{\text{mL-min}} = \frac{V_{\text{mo-min}}}{I_{\text{o-max}}} = \frac{M_{\mathrm{m}} V_{\text{i-min}} V_{\mathrm{o}}}{P_{\text{o-max}}} = 260\Omega. \tag{55}$$

According to Inequalities (51) and (53), by using MATLAB, a three-dimensional graph regarding C_{r}, K, and R_{mL} is obtained as shown in Fig. 12(a). When the DCX is operating between two surfaces, PO mode operation is guaranteed for the DCX. For ensuring that the DCX is always operating in PO mode during a wide load range, a plane R_{mL}=1560 Ω is made, and the intersection line is the red line on the upper surface; similarly, a plane R_{mL}=260 Ω is made, and the intersection line is the blue line on the lower surface. Fig. 11(b) is the overhead view of Fig. 11(a), and the intersection point A shown in Fig. 11(b) can be calculated according to Inequalities (51) and (53); the result is (0.6771uF, 2.8889).

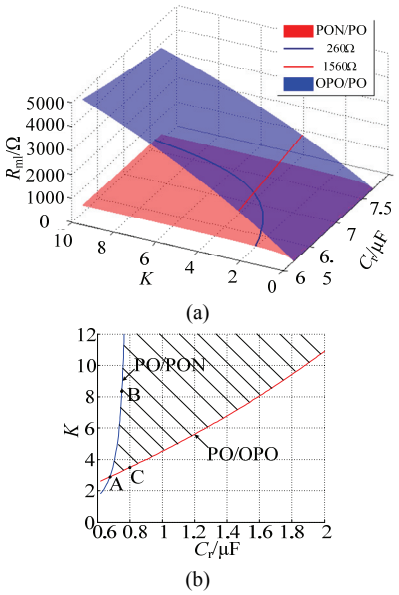

Fig. 12. Boundary conditions among different operating modes.

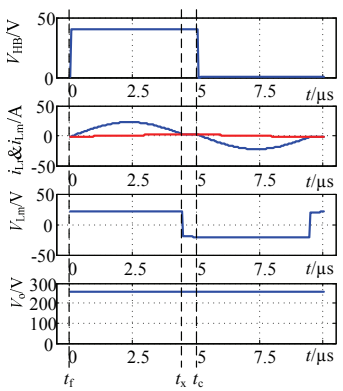

Fig. 13. Simulation waveforms at point B.

To verify the accuracy of the theoretical analysis, point B (0.75uF, 8.21) at the boundary between PON and PO modes and point C (0.8uF, 3.484) at the boundary between OPO and PO modes are selected. At point B, R_{mL}=260 Ω, and L_{r}=2.67uH and L_{m}=21.91uH can be calculated according to the design procedures. At point C, R_{mL}=1560 Ω; similarly, L_{r}=2.85uH and L_{m}=9.94uH can be calculated. In Fig. 13, the simulation waveforms at point B are shown, and the DCX is operating in PO mode; at t_{c}, the voltage across the magnetic inductor $V_{\mathrm{Lm,tc}}$ is $-V_{\mathrm{mo}}/2N$, which means that the DCX is operating at the boundary between the PO and PON modes. Fig. 14 shows the simulation waveforms at point C. Similarly, at t_{f}, the voltage across the magnetic inductor $V_{\mathrm{Lm,tf}}$ is $V_{\mathrm{mo}}/2N$, which means that the DCX is operating at the boundary between the PO and OPO modes. Therefore, the simulation results agree with the theoretical analysis findings.

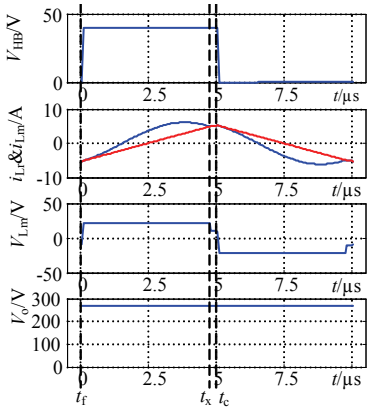

Fig. 14. Simulation waveforms at point C.

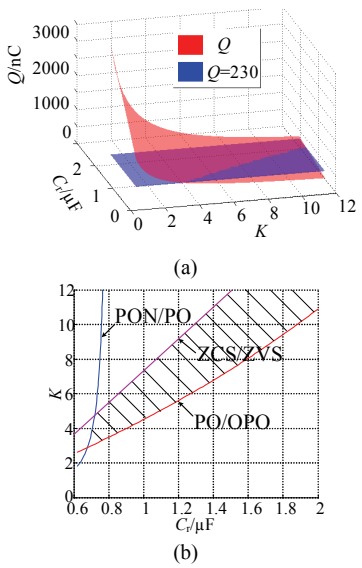

Fig. 15. Boundary condition for soft switching.

To ensure that switches S_{a1} and S_{a2} can achieve ZVS operation, the charge stored in the drain-to-source capacitance C_{ds} of the switch should be extracted completely during the dead time t_{dead}. The resonant current during the dead time is nearly the same as in the P subinterval, and the dead time is extremely shorter than the switch period; thus, the resonant current can be linearized. Therefore, the condition for ZVS operation can be derived as

$$Q=\left[\left|i_{Lr}(0)\right|+\left|i_{Lr}(t_{dead})\right|\right]t_{dead}/2\geq 2C_{ds}V_{i\text{-}max}. \quad (56)$$

In steady state, the output power is confirmed, and the primary side current is constant; thus, if the converter can achieve ZVS operation when the input voltage is at its maximum value, then ZVS operation for the whole operation range can be guaranteed. In this research, the dead time is selected to be 80 *n*s, and C_{ds} is 1.92*n*F; therefore, we can calculate the value on the right side of Inequality (56), which is 230 nF. Then, $i_{Lr(0)}$ and $i_{Lr(tdead)}$ can be calculated according to Equation (16), and ω_r, k_1, and k_2 can be determined on the basis of the proposed design method. Finally, a three-dimensional

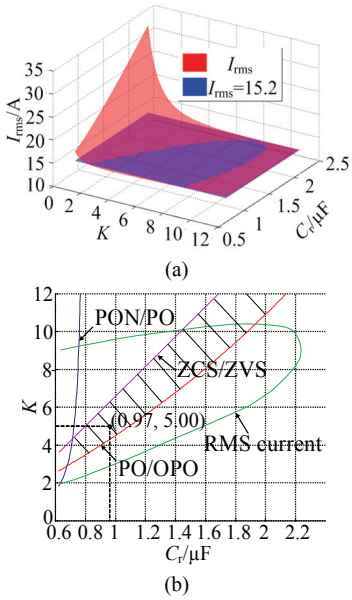

Fig. 16. Limitation of the resonant current.

graph regarding C_r, *K,* and *Q* can be obtained as shown in Fig. 15(a). Fig. 15(b) is obtained by combining the intersection line in Fig. 15(a) with that in Fig. 12(b).

The RMS current of the resonant tank is related to the conduction losses; thus, a limitation on I_{Lr} is required to improve efficiency further. In the following section, FHA is adopted to approximate the limitation value of I_{Lr}.

According to Equation (31), the fundamental voltage RMS value of the half-bridge input voltage can be expressed as

$$V_{HB}=\frac{\sqrt{2}}{\pi}V_i. \quad (57)$$

Given an assumption that the fundamental power factor $\lambda\geq 0.95$, without consideration of the losses, the expression of λ can be derived as

$$\lambda=\frac{V_{mo}I_o}{V_{HB}I_{Lr}}\geq 0.95. \quad (58)$$

According to Equation (58), the limitation for I_{Lr} can be expressed as $I_{Lr}\leq 15.2$ A. On the basis of the design procedures, the RMS value of I_{Lr} can be obtained. Fig. 16(a) shows a three-dimensional graph of C_r, *K,* and RMS current of I_{Lr}. The shaded area of Fig. 16(b) shows the final range of C_r and *K*.

Theoretically, all points in the shaded area can be selected. However, in practice, the following conditions are considered:

1) the commercially available capacitor values and their corresponding voltage stresses;
2) a high *K,* which usually reduces the resonant tank RMS current while increasing in size.

Therefore, a reasonable value based on these considerations must be selected. In the experiment, C_r=0.97*u*F and *K*=5 are selected, and the corresponding resonant components are calculated as

$$\begin{cases} C_r = 0.97\mu F \\ L_r = 2.27\mu H \\ L_m = 11.2\mu H \end{cases}. \quad (59)$$

Based on the input and output of the auxiliary converter, L_a=1mH and C_a=10μF are selected for the auxiliary converter.

V. Experimental Results

A 400 W experimental prototype based on the calculated parameters is built to verify the theoretical analysis. Fig. 17(a) shows the setup of the system, and Fig. 17(b) shows the experimental prototype of the proposed converter. Table I shows the circuit parameters and component part numbers for the proposed converter.

Fig. 18(a) shows the experimental waveforms when the input voltage is 40 V. Under this condition, S_{a1} of the auxiliary converter is always on, the output voltage is regulated by controlling the duty cycle of S_{a2}, the auxiliary converter is working in boost mode, the output voltage V_{ao} is 138 V, and the voltage gain M_a is 3.45. The output voltage of the DCX is 262 V, and its voltage gain M_m is 6.55.

Fig. 18(b) shows the experimental waveforms when the input voltage is 51 V. Under this condition, S_{a1} of the auxiliary converter is operating at a constant duty cycle of 0.8, the output voltage is regulated by controlling the duty cycle of S_{a2}, the auxiliary converter is working in buck-boost mode, the output voltage V_{ao} is 62 V, and the voltage gain M_a is 1.21. The output voltage of the DCX is 338 V, and its voltage gain M_m is 6.62.

Fig. 18(c) shows the experimental waveforms when the input voltage is 54 V. Under this condition, S_{a2} of the auxiliary converter is operating at a constant duty cycle of 0.2, the output voltage is regulated by controlling the duty cycle of S_{a1}, the auxiliary converter is working in buck-boost mode, the output voltage V_{ao} is 44 V, and the voltage gain M_a is 0.81. The output voltage of the DCX is 359 V, and its voltage gain M_m is 6.64.

Fig. 18(d) shows the experimental waveforms when input voltage is 60 V. Under this condition, S_{a2} of the auxiliary converter is always off, the output voltage is regulated by controlling the duty cycle of S_{a1}, the auxiliary converter is working in buck mode, the output voltage V_{ao} is 12 V, and the voltage gain M_a is 0.2. The output voltage of the DCX is 388 V, and its voltage gain M_m is 6.46.

During the whole input voltage range, the auxiliary converter has boost, buck-boost, and buck operation modes, and the voltage gain of the DCX nearly remains constant at 6.5, which agrees with the theoretical analysis. Notably, the resonant inductor current i_{Lr}, which is also the input current of the DCX, almost remains constant. This phenomenon can be explained by power conservation; the output power and output voltage are constant in different conditions, and the output current is constant. Meanwhile, a constant gain conversion is achieved in the DCX; thus, the resonant inductor current depends on the output current.

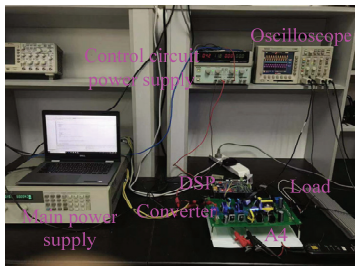

(a)

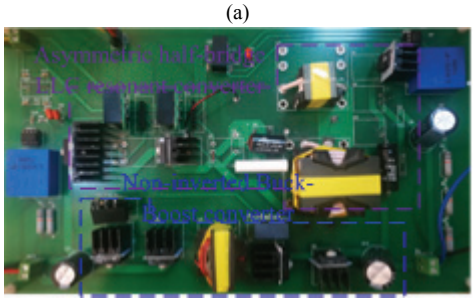

(b)

Fig. 17. Photographs of experimental setup. (a) System setup. (b) Experimental prototype of the proposed converter.

TABLE I
Circuit Parameters and Component Part Numbers

Unit	Components	Parameters
DCX	Resonant capacitor C_r	0.97μF
	Resonant inductor L_r	2.27μH
	Magnetic inductor L_m	11.2μH
	Output capacitor C_{mo1}, C_{mo2}	22μF
	Turns ratio N_m	4:25
	Switch S_{m1}、S_{m2}	IRFP4227
	Diode D_{m1}、D_{m2}	STTH5R06FP
Auxiliary Converter	Inductor L_a	0.6mH
	Output capacitor C_{ao}	22μF
	Switch S_{a1}、S_{a2}	IRFP4227
	Diode D_{a1}、D_{a2}	DSEI30-06A

Fig. 19 shows the ZVS operation of S_{m2} under the most difficult condition for achieving ZVS, that is, when the input voltage reaches its maximum value (V_i=60 V), and the output power reaches its minimum value (P_o=100 W). Before its drive signal Q_{sm2} comes, the resonant current i_{Lr} is positive. Thus, the drain-to-source current of S_{m2} is negative, which means its parallel diode is conducting. Therefore, the voltage across S_{m2} becomes zero, and ZVS operation is achieved. Similarly, S_{m1} can achieve ZVS operation.

Fig. 20 shows the theoretical and experimental results of the ratio of the DCX transmitted power to total power with different input voltages. These results agree with the theoretical analysis findings. Therefore, with increased input voltage, the power transmitted by the DCX increases.

Fig. 21 shows the dynamic response of the proposed converter when the output power changes from full power to half power. The DCX is operating at the resonant frequency

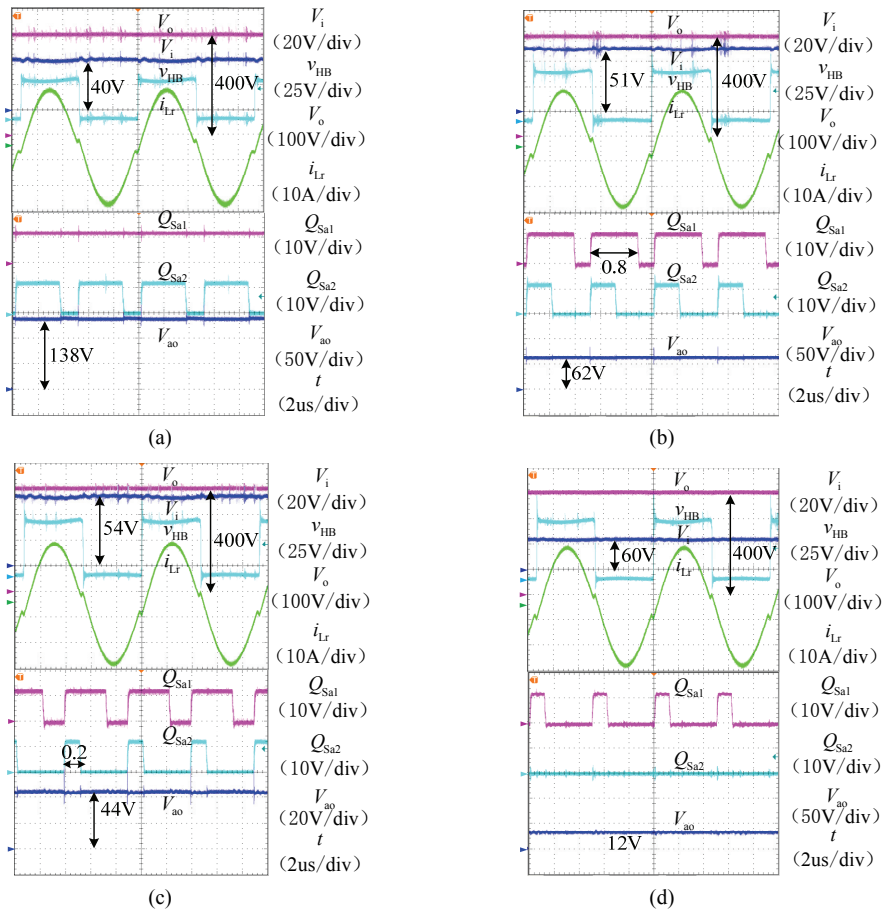

Fig. 18. Experimental waveforms with different input voltages. (a) V_i=40 V. (b) V_i=51 V. (c) V_i=54 V. (d) V_i=60 V.

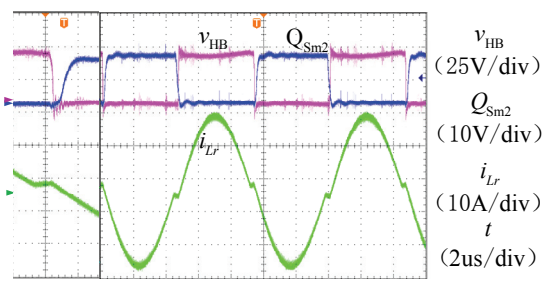

Fig. 19. ZVS operation waveforms of S_{m2} when V_i=60 V and P_o=100 W.

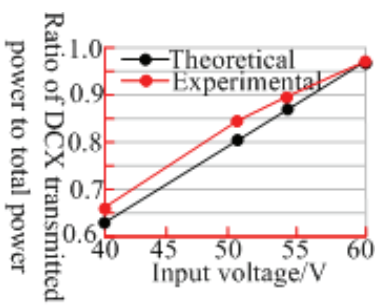

Fig. 20. Theoretical and experimental results of the ratio of the DCX transmitted power to total power with different input voltages.

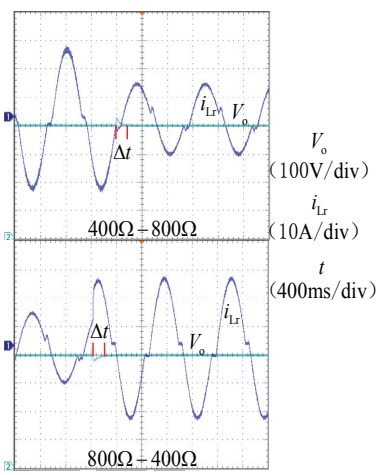

Fig. 21. Dynamic response of the proposed converter when load changes from full power to half power.

operation point; thus, this system is not sensitive to load changes. Therefore, it requires a short time to regulate the output voltage.

Fig. 22 shows the efficiency curves of the system under different input voltages, including auxiliary converter efficiency η_a, DCX efficiency η_{dcx}, and overall efficiency η. η_{dcx} is higher

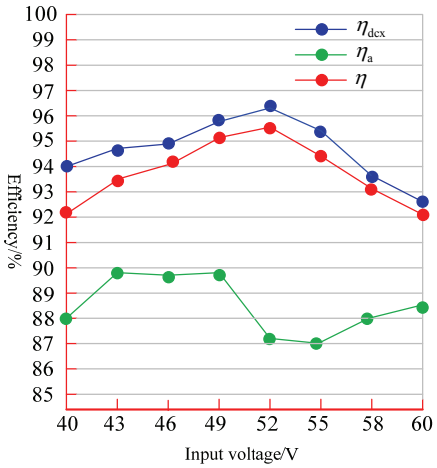

Fig. 22. Efficiency curve with different input voltages.

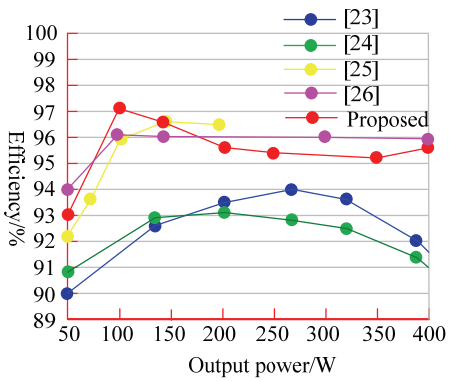

Fig. 23. Efficiency comparison among different topologies.

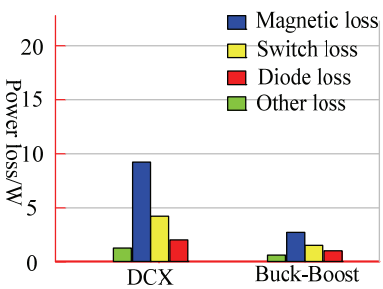

Fig. 24. Power loss distribution when V_i=52 V and P_o=400 W.

than η_a, and with an increase in the input voltage, the difference between η_{dcx} and η becomes smaller. In addition, the system efficiency reaches its highest point at 95.56% when input voltage is 52 V.

Fig. 23 shows the efficiency comparison results among different topologies. The proposed converter has the highest efficiency of nearly 97.2% at 100 W, and with the increase in output power, the efficiency decreases, and the efficiency at rated power (400 W) is approximately 95.56%. The system efficiency is above 95% when the output power is higher than 100 W. The main reason behind this trend is that the converters' losses are proportional to the operating current. Therefore, with the increase in output power, the operating current increases, and the losses increase, leading to low efficiency.

Fig. 24 shows the power loss distribution of the proposed converter with rated output power (400 W) and input voltage V_i=52 V. Clearly, switch loss and magnetic loss are dominant, and both are proportional with the system operating current. This finding can explain why the proposed converter has low efficiency at high output power.

VI. Conclusion

In this study, an input-parallel output-series function decoupling high gain DC/DC converter that consists of a DCX and an auxiliary converter is proposed. The topology selection and control strategy for the DCX and auxiliary converter are discussed. On the basis of the discussion, an optimal design method, which is also the main contribution of this study, is proposed. On the basis of the proposed method, quantitative calculation for the DCX can be achieved, which can guarantee the DCX operating in PO mode; thus, ZVS and ZCS operation for primary switches and secondary diodes can be realized. Meanwhile, by combining with other limitations, the system efficiency can be further optimized. Finally, the quantitative design for the system can be achieved. A simulation and an experiment are implemented to verify the accuracy of the theoretical analysis. The main contribution of this study is summarized as follows:

1) a function decoupling high voltage gain DC/DC converter composed of an LLC resonant converter (acting as a DCX to transfer most of the system's power) and a noninverted buck-boost converter (acting as an auxiliary converter to regulate system output);
2) with the adoption of the function decoupling idea, a constant duty cycle and switching frequency for the LLC resonant converter can be implemented, thereby simplifying the magnetic components and EMI design;
3) instead of a two-mode operation for the noninverted buck-boost converter, a four-mode operation strategy is adopted to avoid extreme duty cycles;
4) an optimal design strategy is proposed. Initially, resonant capacitor C_r and inductor ratio K are selected as input parameters; with the addition of an operation mode boundary limitation (ZVS operation and RMS current limitations), an accurate parameter range is determined.

Acknowledgment

This work was supported in part by the National Natural Science Foundation of China under grant 51577019 and in part by the Graduate Research and Innovation Foundation of Chongqing, China under grant CYB18009.

REFERENCES

[1] Y. Zhang, Y. Xiang and L. Wang, "Power system reliability assessment incorporating cyber attacks against wind farm energy management systems," *IEEE Trans. Smart Grid.*, Vol. 8, No. 5, pp. 2343-2357, Sep. 2017.

[2] K. Tseng and J. Lin, "High step-up DC/DC converter for fuel cell hybrid electric vehicles," in *Proc. International Symposium on Next-Generation Electronics*, pp. 498-501, 2013.

[3] S. Hou, J. Chen, T. Sun, and X. Bi, "Multi-input Step-Up Converters Based on the Switched-Diode-Capacitor Voltage Accumulator," *IEEE Trans. Power Electron.*, Vol. 31, No. 1, pp. 381-393, Jan. 2016.

[4] X. Zhu, B. Zhang, Z. Li, H. Li, and L. Ran, "Extended switched-boost DC-DC converters adopting switched-capacitor/switched-inductor cells for high step-up conversion," *IEEE J. Emerg. Sel. Topics Power Electron.*, Vol. 5, No. 3, pp. 1020-1030, Sep. 2017.

[5] W. Gao, Y. Zhang, X. Lv, and Q. Lou, "Non-isolated high-step-up soft switching DC/DC converter with low-voltage stress," *IET Power Electron.*, Vol. 10, No. 1, pp. 120-128, Jan. 2017.

[6] X. Hu, L. Li, Y. Li, and G. Wu, "Input-parallel output-series DC–DC converter for non-isolated high step-up applications," *Electron. Lett.*, Vol. 52, No. 20, pp. 1715-1717, Sep. 2016.

[7] M. Moradzadeh, S. Hamkari, E. Zamiri, and R. Barzegarkhoo, "Novel high step-up DC/DC converter structure using a coupled inductor with minimal voltage stress on the main switch," *J. Power Electron.*, Vol. 16, No. 6, pp. 2005-2015, Nov. 2016.

[8] B. Honarjoo, S. M. Madani, M. Niroomand, and E. Adib, "Analysis and implementation of a new single switch, high voltage gain DC-DC converter with a wide CCM operation range and reduced components voltage stress," *J. Power Electron.*, Vol. 18, No. 1, pp. 11-22, Jan. 2018.

[9] P. Saadat and K. Abbaszadeh, "A single-switch high step-up DC-DC converter based on quadratic boost," *IEEE Trans. Ind. Electron.*, Vol. 63, No. 12, pp. 7733-7742, Dec. 2016.

[10] S. Lee and H. Do, "High step-up cascade synchronous boost DC–DC converter with zero-voltage switching," *IET Power Electron.*, Vol. 11, No. 3, pp. 618-625, Mar. 2018.

[11] T. J. Liang and K. C. Tseng, "Analysis of integrated boost-flyback step-up converter," *IEE Proceedings - Electric Power Applications*, Vol. 152, No. 2, pp. 217-225, Mar. 2005.

[12] K. Park, G. Moon, and M. Youn, "Nonisolated high step-up boost converter integrated with Sepic converter," *IEEE Trans. Power Electron.*, Vol. 25, No. 9, pp. 2266-2275, Sep. 2010.

[13] A. M. S. S. Andrade, J. C. Giacomini, C. Rech, L. Schuch and M. L. d. S. Martins, "Boost-zeta high step-up PV module integrated converter," in *Proc. ECCE*, pp. 1046-1053, 2015.

[14] T. Lodh and T. Majumder, "High gain and efficient integrated flyback-Sepic DC-DC converter with leakage energy recovery mechanism," in *Proc. SCOPES*, pp. 1495-1500, 2016.

[15] W. Qin, X. Wu, and J. Zhang, "A family of DC transformer (DCX) topologies based on new ZVZCS cells with DC resonant capacitance," *IEEE Trans. Power Electron.*, Vol. 32, No. 4, pp. 2822-2834, Apr. 2017.

[16] X. Wu, H. Chen, and Z. Qian, "1-MHz LLC resonant DC transformer (DCX) with regulating capability," *IEEE Trans. Ind. Electron.*, Vol. 63, No. 5, pp. 2904-2912, May 2016.

[17] X. Fang, H. Hu, Z. J. Shen, and I. Batarseh, "Operation mode analysis and peak gain approximation of the LLC resonant converter," *IEEE Trans. Power Electron.*, Vol. 27, No. 4, pp. 1985-1995, Apr. 2012.

[18] C. Yao, X. Ruan, W. Cao, and P. Chen, "A two-mode control scheme with input voltage feed-forward for the two-switch buck-boost DC–DC converter," *IEEE Trans. Power Electron.*, Vol. 29, No. 4, pp. 2037-2048, Apr. 2014.

[19] N. Zhang, G. Zhang, and K. W. See, "Systematic derivation of dead-zone elimination strategies for the noninverting synchronous buck-boost converter," *IEEE Trans. Power Electron.*, Vol. 33, No. 4, pp. 3497-3508, Apr. 2018.

[20] J. Deng, S. Li, S. Hu, C. C. Mi, and R. Ma, "Design methodology of LLC resonant converters for electric vehicle battery chargers," *IEEE Trans. Veh. Technol.*, Vol. 63, No. 4, pp. 1581-1592, May 2014.

[21] J. Liu, J. Zhang, T. Q. Zheng, and J. Yang, "A modified gain model and the corresponding design method for an LLC resonant converter," *IEEE Trans. Power Electron.*, Vol. 32, No. 9, pp. 6716-6727, Sep. 2017.

[22] J. Deng, C. C. Mi, R. Ma, and S. Li, "Design of LLC resonant converters based on operation-mode analysis for level two PHEV battery chargers," *IEEE Trans. Mechatron.*, Vol. 20, No. 4, pp. 1595-1606, Aug. 2015.

[23] X. Hu and C. Gong, "A high voltage gain DC–DC converter integrating coupled-inductor and diode–capacitor techniques," *IEEE Trans. Power Electron.*, Vol. 29, No. 2, pp. 789-800, Feb. 2013.

[24] S.-M. Chen, T.-J. Liang, L.-S. Yang, and J.-F. Chen, "A cascaded high step-up DC–DC converter with single switch for microsource applications," *IEEE Trans. Power Electron.*, Vol. 26, No. 4, pp. 1146-1153, Apr. 2011.

[25] H. Gui, Z. Zhang, X. He, and Y. Liu, "A high voltage-gain LLC micro-converter with high efficiency in wide input range for PV applications," in *Proc. APEC*, pp. 637-642, 2014.

[26] M. Forouzesh, Y. Shen, K. Yari, Y. P. Siwakoti, and F. Blaabjerg, "High-efficiency high step-up DC-DC Converter with dual coupled inductors for grid-connected photovoltaic systems," *IEEE Trans. Power Electron.*, Vol. 33, No. 7, pp. 5967-5982, Jul. 2018.

Yuqi Wei was born in Henan, China, in 1995. He received his B.S. degree in electrical engineering from Yanshan University, Hebei, China, in 2016 and his M.S. degree in electrical engineering from the University of Wisconsin-Milwaukee (UWM), Wisconsin, U.S.A., in 2018. Currently, he is pursuing his master's degree in Chongqing University, Chongqing, China. His research interests include topology, modeling and control of power converters, and applications for battery charger converter.

Quanming Luo was born in Chongqing, China, in 1976. He received his B.S., M.S., and Ph.D. degrees in electrical engineering from Chongqing University in 1999, 2002, and 2008, respectively. Since 2005, he has been with the College of Electrical Engineering, Chongqing University, where he is currently a professor. He is the author or coauthor of more than 40 papers in journals or conference proceedings. His current research interests include LED driving systems, communication power systems, power harmonic suppression, and power conversion systems in electrical vehicles.

Xingyu Lv was born in Sichuan, China. He received his B.S. and M.S. degrees in electrical engineering from Chongqing University, Chongqing, China, in 2015 and 2018, respectively. His current research interests include high voltage gain DC/DC converters for PV system applications.

Pengju Sun received her B.S. and Ph.D. degrees in electrical engineering from Chongqing University, Chongqing, China, in 2005 and 2011, respectively. Between September 2009 and August 2010, she was a visiting student in the University of California, Irvine in California, U.S.A. Since 2011, she has been with the College of Electrical Engineering, Chongqing University, where she is currently an associate professor. Her research interests include switching power converters, power quality control, and reliability of power converters.

Xiong Du (M'13) obtained his B.S., M.S., and Ph.D. degrees in electrical engineering from Chongqing University, China, in 2000, 2002, and 2005, respectively. He has been with Chongqing University since 2002 and is currently a full professor in its School of Electrical Engineering. He was a visiting scholar at Rensselaer Polytechnic Institute, New York, U.S.A., from July 2007 to July 2008. His research interests include power electronics system reliability and stability. He was a recipient of the National Excellent Doctoral Dissertation of P.R. China in 2008.